Available online at www.sciencedirect.com
SCIENCE DIRECT®
Journal of Solid State Chemistry 178 (2005) 3275–3283
JOURNAL OF SOLID STATE CHEMISTRY
www.elsevier.com/locate/jssc

High-pressure rare earth silicates: Lanthanum silicate with barium phosphate structure, holmium silicate apatite, and lutetium disilicate type X

Michael E. Fleet[a,*], Xiaoyang Liu[a,b]

[a]Department of Earth Sciences, University of Western Ontario, London, Ont., Canada N6A 5B7
[b]State Key Laboratory of Inorganic Synthesis and Preparative Chemistry, College of Chemistry, Jilin University, 2699 Qianjin Street, Changchun 130012, PR China

Received 29 June 2005; received in revised form 11 August 2005; accepted 14 August 2005
Available online 12 September 2005

Abstract

The phase relations of a wide selection of rare earth disilicates have been investigated up to 10 GPa and 1700 °C using piston cylinder and multi-anvil equipment. Single-crystal X-ray structures have been obtained for the following high-pressure phases: (1) $La_{2.67}(SiO_4)_2$: monoclinic, space group $C2/m$, $Z = 2$, $a = 9.419(2)$, $b = 5.445(1)$, $c = 7.214(1)$ Å, $\beta = 115.71(3)°$, $R = 0.042$; disordered $Ba_3(PO_4)_2$ structure type, with $3 \times b$ and $7 \times b$ superstructures identified. (2) $Ho_{8.67}(SiO_4)_6(OH)_2$: hexagonal, $P6_3/m$, $Z = 1$, $a = 9.3221(4)$, $c = 6.7347(2)$ Å, $R = 0.026$; silicate hydroxyapatite. (3) $Lu_2Si_2O_7$: tetragonal, $P4_12_12$, $Z = 4$, $a = 6.5620(2)$, $c = 11.9535(4)$ Å, $R = 0.023$; type X diorthosilicate structure, and the silicate analogue of tetragonal $Er_2Ge_2O_7$.

Keywords: Rare earth silicates; High-pressure phases; Lanthanum silicate; Holmium hydroxyapatite; Lutetium disilicate

1. Introduction

Study of rare earth (*RE*) silicates provides unique insight into the influence of size of the large cation in high-pressure crystal chemistry. Moreover, high-pressure synthesis has the potential for generating new phases and material properties for compounds of this important element series. Eleven different structure types (A–L) have been reported for the single *RE* disilicates [1–20]. This diversity in structure type reflects both the monotonic decrease in size of the RE^{3+} cation through the lanthanide series and crystal-chemical response to change in temperature and pressure. In eight of these structure types (A, B, C, D, E, F, G, H, and K) the SiO_4 tetrahedra are associated into diorthosilicate $[Si_2O_7]^{6-}$ ions, and the structures essentially represent different ways of packing diorthosilicate anions and RE^{3+} cations present in the ratio 1:2. The ninth, tenth and eleventh structure types are not diorthosilicates. Instead, linear trisilicate $[Si_3O_{10}]^{8-}$ ions occur with orthosilicate $[SiO_4]^{4-}$ ions in the type B and L structures [5,14,16,17,20], and a horseshoe-shaped catena-tetrasilicate $[Si_4O_{13}]^{10-}$ ion occurs with two orthosilicate ions per formula unit (pfu) in the type I structure of $La_2Si_2O_7$ [19]. The type B structure has been reported for the disilicates of Eu, Gd, Tb, Dy, Ho, and Er at the lowest temperatures investigated (below 1000–1450 °C) at 1 bar [1] and for Tm disilicate at 900 °C and low pressure [20], as well as for the disilicates of Tm, Yb and Lu at higher pressure (up to 7.0 GPa [21]). Bocquillon et al. [21] also found that a phase with a new structure type (X), which was believed to be the silicate analogue of $Er_2Ge_2O_7$ [22], replaced the type C phase at moderate temperature and, in turn, was replaced by the type B phase at high pressure. Loriers et al. [23] proposed that the phase transition sequence C → X → B is accompanied by closure of the dihedral (Si–O–Si) bond angle with increase in pressure. This suggestion is supported by the report of the high-pressure (10 GPa, 1600–1700 °C) type K structure for the disilicates of Nd, Sm, Eu, and Gd [15], where compression is accomplished

*Corresponding author. Fax: +1 519 661 3198.
E-mail address: mfleet@uwo.ca (M.E. Fleet).

0022-4596/$ - see front matter © 2005 Elsevier Inc. All rights reserved.
doi:10.1016/j.jssc.2005.08.007

mainly by closure of the Si–O–Si bond angle to 123–124°, through rigid body rotation of the two SiO_4 tetrahedra in the diorthosilicate ion. In the present study, we confirm the type X structure for $Lu_2Si_2O_7$ at high pressure, extend the high-pressure phase relations of *RE* disilicates, and discuss the crystal-chemical response to increase in pressure in the phase transition sequence C→D→X→B→L. We also investigate several off-composition products, reporting the subcell structure and complex superstructures for La silicate with the Ba phosphate structure [24], and the structure of a Ho silicate hydroxyapatite [12,25–32].

2. Experimental procedures

2.1. Synthesis and annealing experiments

RE silicates were synthesized largely from oxide mixes using procedures described in earlier studies [14–17,24]. Synthesis experiments yielding investigated *RE* silicate products are summarized in Table 1. The influence of pressure was investigated within the optimum ranges of the available methods of synthesis: i.e., ~1 atm for platinum dish and open capsule, 0.1 GPa for cold-seal hydrothermal, 0.5–4.0 GPa for piston cylinder, and 10 GPa for multi-anvil methods.

Single crystals of $Dy_2Si_2O_7$ type B were encountered as a by-product in a hydrothermal experiment (no. 16) to synthesize crystals of Dy-bearing chlorapatite. A Ca–Dy–silicate starting composition of stoichiometry $Ca_4Dy_6(SiO_4)_6Cl_2$ was prepared from $CaCO_3$, Dy_2O_3, SiO_2, and $CaCl_2$. The charge consisted of about 0.030 g of the starting composition, 0.01 g of NaCl, 0.030 g of a mixture of $CaCl_2 \cdot H_2O$ and P_2O_5 in the stoichiometric proportion of $Ca_{10}(PO_4)_6Cl_2$, and 0.01 g of deionized water contained in a sealed gold capsule 3.5 cm in length. The experiment was performed in a cold-seal bomb, and the products were crystallized by gradient cooling from the melt. Piston-cylinder experiments were performed in an end-loaded

Table 1
Experiments on synthesis of RE disilicates

Expt.	*RE*	Type[a]	*P* (GPa)	*T* (°C)	Time (h)	RE_2O_3:SiO_2	Product[b]
1	La	PC	2	1200	24	2:3	BPO
2	La	PC	4	1450	12	2:3	BPO
3	La	MA	10	1600	24	1:2	BPO + U
4	La	MA	10	1600	24	1:2	BPO + U
5	La	MA	10	1700	12	1:2	BPO + U
6	Ce	PC	1	1550	18	1:2	NoRn
7	Ce	LP	0	1600	24	1:2	G
8	Pr	PC	1	1550	18	1:2	A
9	Nd	MA	10	1600	24	1:2	K
10	Sm	MA	10	1700	12	1:2	K
11	Eu	MA	10	1700	12	1:2	K
12	Gd	PC	0.5	1400	18	1:2	B
13	Gd	PC	2	1400	24	1:2	B
13a	Gd	ANN	0	1300	120		B
13b	Gd	ANN	0	1500	12		E
13c	Gd	ANN	0	1400	45		E
14	Gd	MA	10	1600	24	1:2	K
15	Tb	PC	2	1500	6		B
16	Dy	CSH	0.1	735	13	—	B
17	Dy	MA	10	1600	24	1:2	L
18	Ho	PC	2	1450	5	1:2	AP + B
19	Ho	LP	0	1150	96	1:2	B
20	Ho	PC	2.5	1450	5	1:2	B
21	Ho	PC	4	1450	5	1:2	L
21a	Ho	ANN	0	1100	162		B
22	Tm	PC	2.5	700	5	1:2	X
23	Tm	PC	4	1250	5	1:2	L
23a	Tm	ANN	0	1100	162		X
23b	Tm	ANN	0	1300	24		X
24	Tm	PC	4	1450	5	1:2	L
25	Tm	MA	10	1700	12	1:2	L
26	Lu	PC	2	1450	5	1:2	D
27	Lu	PC	4	1200	5	1:2	X
28	Lu	MA	10	1600	24	1:2	L

[a]PC is piston cylinder; MA is multi-anvil; ANN is high-pressure product annealed at low pressure; LP is low pressure with Pt capsule in sealed silica glass tube; CSH is cold-seal, hydrothermal.

[b]BPO is derivative barium phosphate; AP is silicate apatite; K, B, E, D, X, L are RE disilicates identified by structure type; U is uncharacterized material; NoRn is no reaction.

apparatus, and were quenched at pressure by switching off the furnace. Pressure was calibrated from melting of dry NaCl at 1050 °C [33] and the transformation of quartz to coesite at 500 °C [34], and temperature was measured by inserting a Pt–Pt90%Rh10% thermocouple into the high-pressure cell. All furnace parts were previously fired at 1000 °C in air. Charges consisted of oxide mixes + 1–5 wt% H_2O encapsulated in a sealed platinum tube with a diameter of 5 mm and a height of 12 mm, and separated by MgO powder from a graphite tube. For the synthesis of $Tb_2Si_2O_7$ (experiment 15), a small excess of *RE* oxide was added to compensate for the presence of both Tb_2O_3 and TbO_2 in the commercial oxide. Multi-anvil experiments used the MA6/8 superpress at the University of Alberta, Edmonton. A typical synthesis experiment was run in a Pt capsule within a 14 M assembly using a $LaCrO_3$ furnace [35], and monitored with a $W_{95}Re_5$–$W_{74}Re_{26}$ thermocouple. All furnace parts were previously fired at 1000 °C in air. Starting oxide mixes were pre-reacted at 950 °C for 2 h in Pt crucibles, and H_2O was added in most experiments before sealing the capsule. Temperature was quenched by switching off the power to the furnace at the experimental pressure; the quench rate at high pressure was estimated to be about 1000 °C/s. Small amounts of Gd, Ho and Tm disilicate products were contained in Pt crucibles, and annealed in air in a high-temperature furnace (Table 1). Miscellaneous low-pressure syntheses were made with starting mixtures in Pt capsules either supported in ceramic crucibles or in evacuated sealed silicate glass tubes.

The experimental products were characterized by petrographic optical microscopy, single-grain Gandolfi, powder, and single-crystal X-ray diffraction, and, selectively, by electron probe microanalysis, using a JEOL 8600 Superprobe. The electron probe microanalyser was operated at an accelerating voltage of 20 kV, a beam current of 15 nA, a beam diameter of 2 μm, and 20 s counts, using silicate and *RE* phosphate standards, and the measurements were reduced using the Love–Scott model [36]. Analysis of crystal fragments resulted in formulae of $La_{2.46}Si_{2.00}O_{7.70}$ ($n = 10$ spots) for La silicate with the Ba phosphate (BPO) structure, $Ho_{8.97}Si_{6.00}O_{25.45}$ ($n = 16$) for Ho silicate apatite (experiment 18), and $Lu_{1.96}Si_{2.03}O_7$ ($n = 20$) for Lu disilicate-type X (experiment 27); the small discrepancies with the assumed ideal formulae of $La_{2.67}(SiO_4)_2$, $Ho_{8.67}(SiO_4)_6(OH)_2$ and $Lu_2Si_2O_7$, respectively, are interpreted as artifacts of the analytical method used.

2.2. X-ray structures

Single-crystal fragments were reduced in size and shaped by trimming with a scalpel blade, and evaluated for X-ray structure analysis by optical petrography and X-ray precession photography and diffractometry. Single-crystal measurements were made at room temperature and pressure with a Bruker Kappa CCD diffractometer and graphite-monochromatized Mo$K\alpha$ X-radiation (50 kV, 32 mA, $\lambda = 0.71069$ Å). The COLLECT Nonius software was used for unit-cell refinement and data collection. The reflection data were processed with SORTAV-COLLECT, using an empirical procedure for absorption correction, and SHELXTL/PC [37] and Fourier methods were used for structure determination. Structure refinements were made with LINEX77 (State University of New York at Buffalo), using scattering factors for neutral atomic species and values of f' and f'', respectively, from Tables 2.2A and 2.3.1 of the *International Tables for* X-ray *Crystallography* [38].

3. Discussion

3.1. BPO-type lanthanum silicate

Experiments with La disilicate starting composition at 10 GPa yielded a mixture of a phase with Ba phosphate (BPO)-type structure of ideal formula $La_{2.67}(SiO_4)_2$ and fine-grained uncharacterized material, rather than single-phase high-pressure disilicate [24] (Table 1). Liu and Fleet [24] reasoned that the stable high-pressure assemblage was BPO silicate + melt. They reported a monoclinic unit cell with $a = 5.463$, $b = 16.382$, $c = 7.429$ Å, and $\beta = 115.78°$ and space group $C2/m$, but the structural details were elusive. In the present study, the BPO phase was the only identified product in piston cylinder experiments at 2–4 GPa using a more La-rich starting composition (i.e., $2La_2O_3 \cdot 3SiO_2$), and experiments with Ce and Pr disilicate starting compositions yielded only type G and A disilicates at 1 bar and 1 GPa, respectively (Table 1).

Two crystals from the multi-anvil experiment 3 and one each from the piston cylinder experiments 1 and 2 were studied by single crystal X-ray diffractometry (Table 2). When the reflection data were processed by the XPREP programme package of SHELXTL, it was evident that the seemingly unrelated unit cells from the Bruker Kappa diffractometer could be transformed to a series of monoclinic superstructures representing partial ordering of La^{3+} cations and vacancies in the *b*-axis direction. Experiment 1 yielded the monoclinic subcell (labelled 1B), experiment 3 the $3 \times b$ (3B) superstructure and experiment 2 the $7 \times b$ (7B) superstructure. The monoclinic (m) subcell bears a simple relationship to the hexagonal (rhombohedral; r) unit cell of the BPO structure (Fig. 1), with $a_m = a_r\sqrt{3}$, $b_m = a_r$, $c_m = (c_r/3)/\cos\theta$ and $\beta = (\pi/2) + \theta$, where $\theta = \tan^{-1}(a_r\sqrt{3}/c_r)$. Surprisingly, the intensities of the superstructure reflections were highly variable between crystal products from the same experiment and from one experiment to another. This variability is well illustrated by powder X-ray diffraction patterns simulated from the single-crystal reflection data using SHELXTL (Fig. 2). The 3B superstructure is only weakly developed in the two crystals from experiment 3, and superstructure reflections are more prominent in the first crystal (by a factor of about $\times 2$) than in the second. On the other hand, the 7B superstructure is strongly developed in the only crystal investigated from experiment 2, but this superstructure is not evident in a powder X-ray diffraction pattern of the

Table 2
Monoclinic superstructures of La silicate with $Ba_3(PO_4)_2$ structure

Super-structure	Expt.[a]	Cell method	a (Å)	b (Å)	c (Å)	α (°)	β (°)	γ (°)
1B	1	Bruker	5.4412(6)	5.4384(7)	7.2138(9)	67.935(6)	67.950(6)	60.063(6)
		Shelxtl	9.419(2)	5.445(1)	7.214(1)	90.0	115.71(3)	90.0
3B	3	Bruker	7.2476(7)	9.0691(8)	9.4538(7)	110.300(5)	102.485(5)	110.234(5)
		Shelxtl	9.450(2)	16.388(3)	7.248(1)	90.0	115.79(3)	90.0
3B	3	Bruker	9.4530(9)	16.382(2)	7.2487(6)	90.0	115.780(5)	90.0
		Shelxtl	9.453(2)	16.382(3)	7.249(1)	90.0	115.78(3)	90.0
7B	2	Bruker	7.2102(3)	9.0616(4)	19.651(1)	99.598(2)	95.972(2)	110.260(3)
		Shelxtl	9.426(2)	38.154(8)	7.210(1)	90.0	115.60(3)	90.0

[a]cf. Table 1; two crystals investigated from experiment 3.

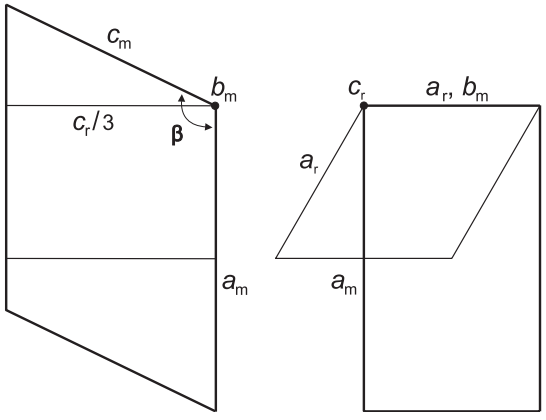

Fig. 1. Relationship of the monoclinic (m) subcell of $La_{2.67}(SiO_4)_2$ to the hexagonal (rhombohedral; r) unit cell of $Ba_3(PO_4)_2$ (BPO) structure.

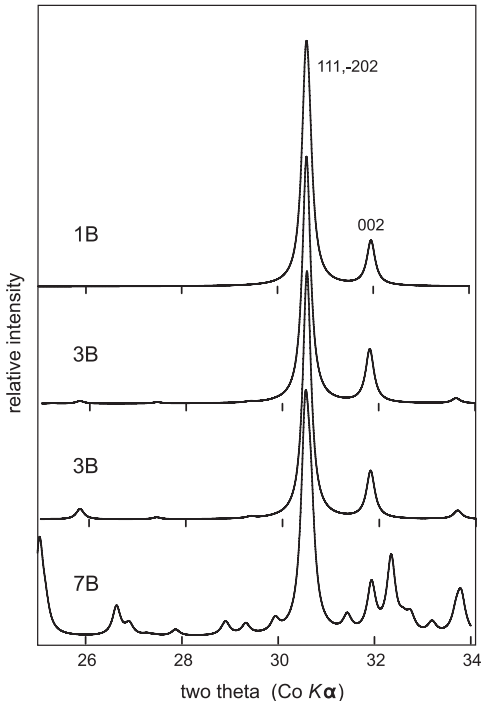

Fig. 2. Powder X-ray diffraction patterns of BPO-type $La_{2.67}(SiO_4)_2$ simulated from single-crystal reflection intensity data for the monoclinic $C2/m$ 1B ($1 \times b$) subcell and 3B ($3 \times b$) and 7B ($7 \times b$) superstructures.

bulk sample. Based on these limited results, it appears that different crystals from the same experiment have the same superstructure but developed to different extents. Also, superstructures are not evident in powder patterns of bulk samples but are present in selected single crystals. These observations suggest that the 1B structure of experiment 1 is disordered and probably represents the quenched high temperature (and high pressure) structural state of the BPO phase. Incipient ordering occurred sporadically during quenching of other experiments, but was restricted by the sluggish mobility of La^{3+} cations and vacancies.

The present investigation of the crystal structures of the monoclinic superstructures resulted only in confirmation of the underlying structure type and rudimentary insight into structural features. These difficulties in structure determination were no doubt related to the incipient ordering and structural heterogeneity of the crystals. However, refinements of the disordered BPO-derivative structure of the crystal from experiment 1 converged satisfactorily in both rhombohedral ($R\bar{3}m$) and monoclinic ($C2/m$) space groups (Table 3). The charge-balanced formula of $La_{2.67}(SiO_4)_2$ was adopted for structure determination and initial structure refinement. Refinement of the rhombohedral structure using anisotropic displacement parameters indicated extensive local disorder of La(1), La(2) and O(1) perpendicular to the c-axis. The refinement was continued using isotropic thermal parameters for all atoms and allowing La(1), La(2) and O(1) to disorder in equipoint 18 h. The monoclinic subcell structure was refined similarly, except that it was now evident that the disorder of La(2) was best described by two well separated areas of electron density; La(2A) with relaxed equipoint symmetry and a satellite position La(2B). Site occupancy refinements showed that the large cation vacancies were essentially restricted to La(2) positions (Table 3). Resulting La/Si ratios were 1.23(1) for both rhombohedral and monoclinic structures, in excellent agreement with the electron probe microanalysis value of 1.23(1).

Table 3
La silicate with $Ba_3(PO_4)_2$ structure: positional and isotropic thermal parameters for average structures

Atom	Equipoint		Occupancy	x	y	z	U_{eq}
	BPO	Refined					
Space group $R\bar{3}m$							
La(1)	3a	18h	0.96(1)	0.0560(6)	0.0280(6)	0.0	0.0145(8)
La(2)	6c	18h	0.747(8)	0.0684(5)	0.0342(5)	0.20087(6)	0.087(7)
Si	6c	6c	1.0	0.0	0.0	0.4062(2)	0.009(1)
O(1)	6c	18 h	1.0	0.037(8)	0.019(8)	0.3216(6)	0.027(5)
O(2)	18h	36i	1.0	0.517(3)	0.526(3)	0.2343(2)	0.021(2)
Space group $C2/m$							
La(1)	3a	8j	0.956(8)	0.0204(2)	0.0358(4)	0.0	0.0114(6)
La(2A)	6c	8j	0.511(9)	0.2165(4)	0.0500(5)	0.6021(2)	0.0107(8)
La(2B)		4i	0.240(8)	0.1667(8)	0.0	0.6057(4)	0.011(1)
Si	6c	4i	1.0	0.4055(4)	0.0	0.2158(5)	0.0111(9)
O(1)	6c	4i	1.0	0.3219(9)	0.0	0.964(1)	0.042(3)
O(2)	18h	4i	1.0	0.2708(7)	0.0	0.295(1)	0.025(2)
O(3)		8j	1.0	0.9865(5)	0.257(1)	0.7038(8)	0.027(2)

Notes: (1) Experiment 1 (Table 1); crystal—$0.050 \times 0.060 \times 0.070\,mm^3$, equant. (2) Space group $R\bar{3}m$: $a = 5.4398(8)$ Å, $c = 19.500(4)$ Å; reflections—2 2 0 unique, 135 with $I < 3\sigma_{(I)}$, $R_{int} = 0.053$; $R = 0.030$; $R_w = 0.040$; $s = 1.139$; $\Delta\rho = +0.98, -10.86\,e\,Å^{-3}$. (3) Space group $C2/m$: reflections—544 unique, 326 with $I < 3\sigma_{(I)}$, $R_{int} = 0.033$; $R = 0.042$; $R_w = 0.039$; $s = 1.521$; $\Delta\rho = +1.36, -1.35\,e\,Å^{-3}$. (4) BPO is $Ba_3(PO_4)_2$.

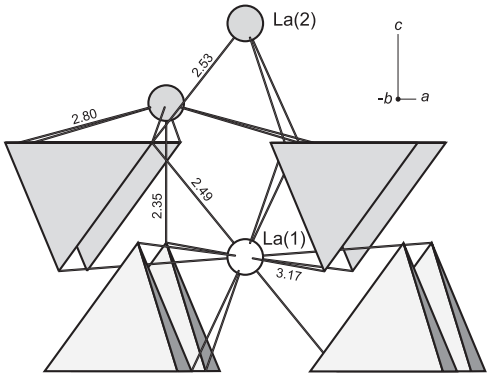

Fig. 3. Stereochemical environment of La(1) (open circle) and La(2) (shaded circles) in the "ideal" structure of rhombohedral BPO-type $La_{2.67}(SiO_4)_2$, calculated with x and y atomic coordinates of O(2) (Table 3) constrained to 0.5.

The ideal BPO structure is layered in the hexagonal (rhombohedral) (001) plane. Two layers of orthophosphate tetrahedra enclose a layer of Ba(1) cations (Fig. 3). Ba(1) is in 12-fold coordination, with an inner sphere of basal tetrahedral oxygen atoms in the configuration of a stretched octahedron and an equatorial outer ring of apical tetrahedral oxygens. These three-layer units are interconnected by a double layer of Ba(2) in 10-fold coordination. Ba(2) is bonded mainly to basal tetrahedral oxygens: four shorter Ba(2)–O bonds represent an inner sphere of oxygens forming a trigonally stretched tetrahedron, and there is an approximately equatorial outer ring of six basal oxygens. The difference between inner and outer sphere bond distances is marginal for $Ba_3(PO_4)_2$, because of the large size of the Ba^{2+} cation, but clearly evident in $Sr_3(PO_4)_2$ [39], and is quite pronounced for the ideal rhombohedral structure of high-pressure La silicate (Fig. 3), where we have a somewhat smaller La^{3+} cation coupled with a somewhat larger SiO_4 tetrahedron; the effective ionic radii for eight-fold coordination of Ba^{2+}, Sr^{2+} and La^{3+} with oxygen are 1.42, 1.25 and 1.18 Å, respectively [40]. The ideal La–O bond distances are considerably distorted in the monoclinic BPO La silicate structure (Table 4). Note that Table 4 includes only bond

Table 4
Selected bond distances and angles for monoclinic BPO La silicate

Bond		(Å)	Bond/angle		(Å/°)
La(1)–O(2)		2.405(6)	La(2A)–O(1)		2.369(9)
La(1)–O(2)^{I}		2.652(6)	La(2A)–O(2)		2.492(9)
La(1)–O(3)^{II}		2.351(6)	La(2A)–O(3)^{IV}		2.768(5)
La(1)–O(3)^{III}		2.572(6)	La(2A)–O(3)^{V}		2.477(5)
La(1)–O(3)^{IV}		2.689(6)	La(2A)–O(2)^{IX}		3.075(3)
La(1)–O(3)^{V}		2.478(6)	La(2A)–O(2)^{X}		2.547(4)
La(1)–O(1)^{VI}		2.97(1)	La(2A)–O(3)^{XI}		2.807(7)
La(1)–O(1)^{VII}		3.087(5)	La(2A)–O(3)^{XII}		3.067(7)
La(1)–O(1)^{VIII}		2.885(5)	La(2A)–O(3)^{XIII}		2.816(6)
Mean		2.677	La(2A)–O(3)^{XIV}		2.547(6)
			Mean		2.697
Si–O(1)		1.64(1)	O(1)–Si–O(2)		108.9(4)
Si–O(2)		1.60(1)	O(1)–Si–O(3)	× 2	108.8(3)
Si–O(3)^{XV}	× 2	1.615(5)	O(2)–Si–O(3)	× 2	110.1(3)
Mean		1.62	O(3)–Si–O(3)^{XVI}		109.9(4)

Notes: Symmetry codes: (I) $-x, -y, -z$; (II) $x-1.0, y, z-1$; (III) $x-1.0, -y, z-1$; (IV) $1.0-x, -y, 1.0-z$; (V) $1.0-x, y, 1.0-z$; (VI) $x, y, z-1.0$; (VII) $x-0.5, 0.5+y, z-1.0$; (VIII) $0.5-x, 0.5+y, 1.0-z$; (IX) $0.5-x, -y-0.5, 1.0-z$; (X) $0.5-x, -y+0.5, 1.0-z$; (XI) $x-1.0, y, z$; (XII) $x-1.0, -y, z$; (XIII) $x-0.5, y-0.5, z$; (XIV) $x-0.5, 0.5-y, z$; (XV) $1.5-x, 0.5-y, 1.0-z$; (XVI) $1.5-x, y-0.5, 1.0-z$.

distances for the reference La(1) and La(2A) positions; the relaxed equipoint symmetry results in slightly different values for each of the locally disordered atoms.

3.2. Holmium silicate hydroxyapatite

Minor apatite occurred as a by-product in some experiments, reflecting the small quantity of water added to the starting mixtures to promote the crystallization of disilicates. Final structural parameters for the Ho apatite of experiment 18 (Table 1) are given in Table 5 and selected bond distances and angles in Table 6. The structure refinement assumed the charge-balanced formula of $Ho_{8.67}(SiO_4)_6(OH)_2$. An isotropic displacement parameter was used for the oxygen atom in the apatite channel [O(4)], and the H atom was assumed to ride on O(4). Bond distances and Ho site occupancies are in good agreement with literature studies on *RE* silicate apatites [12,26–32], for which charge-balancing vacancies and alkali metal cations are essentially restricted to the nine-coordinated Ca(1) position of the hexagonal ($P6_3/m$) apatite-type structure. Ca(2), on the other hand, which lines the wall of the apatite channel and offers a somewhat smaller cation position, tends to be fully occupied by RE^{3+} cations in these structures. The O–H bond length of 1.1 Å resulting from independent refinement of the H atom and the favorable charge balance from the Ho(1) site occupancy confirm that the apatite phase of experiment 18 is hydroxyapatite.

Table 5
Atomic coordinates and equivalent isotropic displacement parameters (Å^2) for holmium silicate hydroxyapatite [$Ho_{8.67}(SiO_4)_6(OH)_2$]

Atom	Site occupancy	x	y	z	U_{eq}
Ho(1)	0.715(2)	2/3	1/3	0.00034(3)	0.0155(5)
Ho(2)	0.967(3)	0.99415(5)	0.23486(5)	1/4	0.0126(2)
Si	1.0	0.3732(3)	0.3998(3)	1/4	0.0124(5)
O(1)	1.0	0.4882(8)	0.3177(8)	1/4	0.026(1)
O(2)	1.0	0.4738(8)	0.5974(8)	1/4	0.023(2)
O(3)	1.0	0.2493(6)	0.3377(7)	0.0628(6)	0.034(1)
O(4)	1.0	0	0	0.221(3)	0.015(4)[a]
H	1.0	0	0	0.05(3)	0.015(4)[a]

Notes: Experiment 18 (Table 1); crystal—$0.045 \times 0.045 \times 0.055\,mm^3$, equant; $a = 9.3221(4)$ Å, $c = 6.7347(2)$ Å; space group $P6_3/m$; reflections—540 unique, 227 with $I < 3\sigma_{(I)}$, $R_{int} = 0.041$; $R = 0.026$; $R_w = 0.020$; $s = 1.211$; $\Delta\rho = +2.25, -1.33\,e\,Å^{-3}$; $U_{eq} = (1/3)\sum_i\sum_j U^{ij}\mathbf{a}^i\mathbf{a}^j a_i.a_j$.
[a]Isotropic refinement.

Table 6
Selected bond distances and angles for holmium silicate hydroxyapatite

Bond		(Å)	Bond/angle		(Å/°)
Ho(1)–O(1)	× 3	2.318(4)	O(4)–H		1.1(2)
Ho(1)–O(2)^{I}	× 3	2.412(4)			
Ho(1)–O(3)^{I}	× 3	2.793(6)	Si–O(1)		1.599(7)
Mean		2.508	Si–O(2)		1.595(7)
			Si–O(3)	× 2	1.609(4)
Ho(2)–O(1)		2.658(6)	Mean		1.603
Ho(2)–O(2)^{II}		2.357(6)			
Ho(2)–O(3)	× 2	2.270(4)	O(1)–Si–O(2)		113.9(3)
Ho(2)–O(3)^{III}	× 2	2.426(4)	O(1)–Si–O(3)	× 2	111.1(2)
Mean		2.401	O(2)–Si–O(3)	× 2	108.5(3)
Ho(2)–O(4)		2.226(2)	O(3)–Si–O(3)^{IV}		103.1(3)

Notes: Symmetry codes. (I) $-x, -y, -z$; (II) $1+(y-x), -x, z$; (III) $1+x, y, z$; (IV) $x, y, 0.5-z$.

Table 7
Atomic coordinates and equivalent isotropic displacement parameters (Å^2) for $Lu_2Si_2O_7$ type X

Atom	x	y	z	U_{eq}
Lu	0.87627(6)	0.35177(6)	0.13411(3)	0.0083(2)
Si	0.9023(4)	0.1536(4)	0.6222(2)	0.0075(5)
O(1)	0.815(2)	$1-x$	3/4	0.012(4)
O(2)	0.0700(8)	0.972(1)	0.6267(8)	0.009(2)
O(3)	0.0528(9)	0.3364(9)	0.5725(5)	0.008(2)
O(4)	0.6958(8)	0.1386(9)	0.5489(5)	0.009(1)

Notes: Experiment 27 (Table 1); crystal—$0.025 \times 0.030 \times 0.035\,mm^3$, equant; $a = 6.5620(2)$, $c = 11.9535(4)$ Å; space group $P4_12_12$; reflections—492 unique, 169 with $I < 3\sigma_{(I)}$, $R_{int} = 0.042$; $R = 0.023$; $R_w = 0.017$; $s = 1.095$; $\Delta\rho = +1.67, -1.49\,e\,Å^{-3}$; $U_{eq} = (1/3)\sum_i\sum_j U^{ij}\mathbf{a}^i\mathbf{a}^j a_i a_j$.

3.3. Type X structure

Final parameters and other relevant experimental details for the Lu disilicate type X of experiment 27 (Table 1) are given in Table 7 and selected bond distances and angles in Table 8; a view of the type X structure is given in Fig. 4. The present independent structure analysis confirms that $Lu_2Si_2O_7$ type X is the silicate analogue of tetragonal $Er_2Ge_2O_7$ [22]. The earlier assignment of the germanate structure to type X Tm, Yb and Lu disilicate was based on unit-cell parameter and X-ray powder pattern data [21,23]. The present unit-cell parameters of $Lu_2Si_2O_7$ type X [$a = 6.5620(2)$, $c = 11.9535(4)$ Å] are in good agreement with those of Bocquillon et al. [21] [$a = 6.565(5)$, $c = 11.95(1)$ Å], and the single-crystal reflection intensities establish the space group as $P4_12_12$. Interestingly, there is a very close correspondence between the stereochemical features of $Lu_2Si_2O_7$ type X and tetragonal $Er_2Ge_2O_7$. The two structures differ mainly in the greater size of the RE^{3+} and T^{4+} cations in $Er_2Ge_2O_7$, but otherwise have very similar REO_7 polyhedra and TO_4 tetrahedral distortions (Table 8). The T–O distances and O–T–O angles are modulated very largely by bond distance/bond strength considerations, as shown by the calculated bond-valence sums in Table 9. For example, O(2) and O(4) are each shared with one T^{4+} and two RE^{3+} cations and would be underbonded if all T–O distances were of average length. The differential shortening of the T–O(2) and T–O(4) bond distances results in a more equitable distribution of bond-valence sums, but opens the O(2)–T–O(4) bond angle, to

Table 8
Bond distances (Å) and angles (°) in $Lu_2Si_2O_7$ type X and tetragonal $Er_2Ge_2O_7$

	$Lu_2Si_2O_7$ (this study)	$Er_2Ge_2O_7$ [22]
a (Å)	6.5620(2)	6.778
c (Å)	11.9535(4)	12.34
V (Å^3)	514.7	566.9
RE–O(2)	2.157(6)	2.195
RE–O(2)^{I}	2.322(6)	2.371
RE–O(3)	2.224(6)	2.278
RE–O(3)^{II}	2.352(6)	2.421
RE–O(3)^{III}	2.510(6)	2.516
RE–O(4)	2.212(6)	2.216
RE–O(4)^{II}	2.245(5)	2.266
⟨*RE*–O⟩	2.289	2.323
T–O(1)	1.643(4)	1.756
T–O(2)^{IV}	1.622(6)	1.733
T–O(3)^{IV}	1.663(6)	1.754
T–O(4)^{V}	1.617(6)	1.751
⟨*T*–O⟩	1.636	1.749
O(1)–*T*–O(2)^{VI}	107.2(4)	110.1
O(1)–*T*–O(3)^{VII}	116.7(6)	113.7
O(1)–*T*–O(4)^{V}	102.7(5)	101.1
O(2VI)–*T*–O(3)^{VII}	98.0(3)	95.0
O(2VI)–*T*–O(4)^{V}	122.8(4)	125.1
O(3VII)–*T*–O(4)^{V}	110.4(3)	112.4
T–O(1)–*T*	141.1(2)	136.0

RE = Lu, Er; *T* = Si, Ge.
Symmetry codes: (I) 1.5−x, 0.5+y, 0.5−z; (II) 1.5−y, x−0.5, 0.5+z; (III) 1.5−x, y−0.5, 0.5−z; (IV) 1−x, 1−y, 0.5+z; (V) 1−y, 1−x, 0.5+z; (VI) 2−x, −y, 0.5+z; (VII) 2−x, 1−y, 0.5+z.

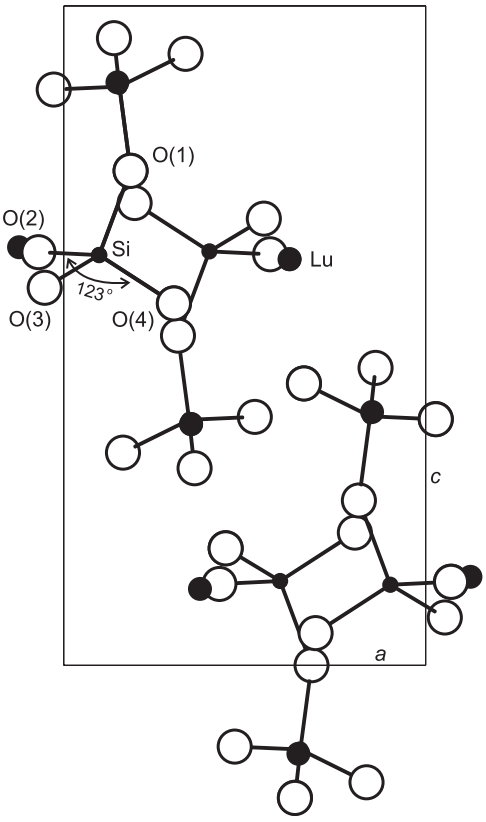

Fig. 4. Partial structure of the tetragonal type X polymorph of $Lu_2Si_2O_7$, showing packing of four diorthosilicate units viewed in *b*-axis (a_2-axis) projection: small solid circles are Si and medium solid circles are Lu.

123° in $Lu_2Si_2O_7$ and 125° in $Er_2Ge_2O_7$. An analogous discussion is given for tetragonal $Er_2Ge_2O_7$ in Smolin [22] based on bond polarization considerations. The dihedral, *T*–O(1)–*T*, bond angle in $Lu_2Si_2O_7$ type X is 141°, which is somewhat greater than that predicted by Loriers et al. [23] and more consistent with the trends for progressive decrease in bridging-oxygen bond angle with increase in size of RE^{3+} cation and pressure of synthesis outlined in Fleet and Liu [15,16].

3.4. High-pressure phase relations

The results of the present experiments on high-pressure synthesis and low-pressure annealing of the *RE* disilicates are summarized in Table 1 and, for $Lu_2Si_2O_7$, are compared with the *P*–*T* phase diagram of Bocquillon et al. [21] in Fig. 5. The high-pressure polymorphism of the *RE* disilicates is driven by increase in the coordination of the RE^{3+} cation (and probably of Si as well [17]) and decrease in the bridging-oxygen bond angle(s) with increase in pressure [15–17,23,24]. It is evident that, even at low pressure [18,19], the diorthosilicates of La have a restricted field of stability, since at 2, 4 and 10 GPa the bulk composition $La_2O_3 \cdot 2SiO_2$ does not crystallize a La disilicate. It appears that polymerized silicate ions are just too bulky to pack with the larger RE^{3+} cations to give coordination numbers greater than, say, 8 or 9. Unfortunately, the pressure stability of Ce and Pr disilicates was not investigated above 1 GPa.

Table 9
Bond-valence sums

$Lu_2Si_2O_7$

	Lu			Si		Σ
O(1)	—	—	—	0.95	0.95	1.90
O(2)	0.61	0.39	—	1.01		2.01
O(3)	0.51	0.36	0.23	0.90		2.00
O(4)	0.48	0.52	—	1.02		2.02
Σ		3.10		3.88		

$Er_2Ge_2O_7$

	Er			Ge		Σ
O(1)	—	—	—	0.98	0.98	1.96
O(2)	0.61	0.38	—	1.04		2.03
O(3)	0.49	0.33	0.26	0.98		2.06
O(4)	0.50	0.57	—	0.99		2.06
Σ		3.14		3.99		

Note: Bond-valence parameters [41].

The present direct syntheses of the type D and X polymorphs of $Lu_2Si_2O_7$ are in good agreement with the

phase relations of Bocquillon et al. [21] (Fig. 5). The detailed phase relations of $Tm_2Si_2O_7$ in that earlier study may be suspect because annealing of the type L polymorph

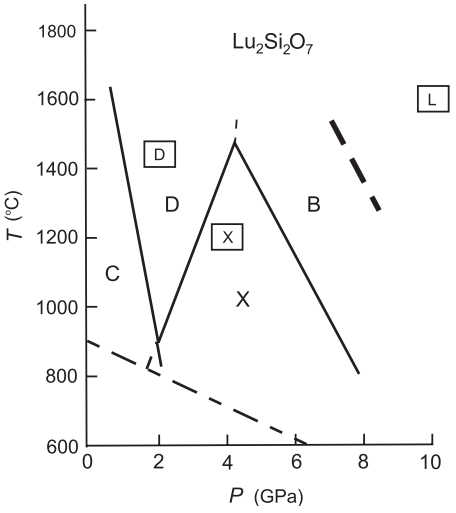

Fig. 5. *P–T* conditions for the high-pressure synthesis of the type D, X, and L polymorphs of Lu disilicate (upper-case letters enclosed by boxes; Table 1), compared with the polymorphic phase relations of Bocquillon et al. [21].

of $Tm_2Si_2O_7$ at 1100 and 1300 °C yielded the type X polymorph in the stability field of the type C polymorph, and Hartenbach et al. [20] reported synthesis of the type B polymorph at 900 °C and low pressure from reaction of Tm, S, RbCl, and vitreous SiO_2 in a sealed silica glass tube. On the other hand, the *P–T* diagram for $Lu_2Si_2O_7$ has a similar morphology to that of $Yb_2Si_2O_7$ [21] and, thus, appears to represent equilibrium phase relations, even though reversal of reaction has not been demonstrated.

The type L structure is adopted by the heavy *RE* disilicates for synthesis at pressures of 4–10 GPa, which is generally beyond the pressure range of the type B structure (Fig. 5). Fleet and Liu [17] noted that this new structure is assembled from alternate (001) strips of the type B structure and a sheared structure containing structural elements (i.e., linear trisilicate $[Si_3O_{10}]^{8-}$ and orthosilicate $[SiO_4]^{4-}$ ions) found in the type B structure but with Si distributed with 50% occupancy over two face-sharing tetrahedra. Not surprisingly, there is a close correspondence between the unit-cell parameters of the type B and L structures, with *a* and *b* closely comparable in the two structures, and *c* and *V* larger by about $\times 1.5$ in the type L structure. The powder X-ray diffraction patterns of the two polymorphs are superficially similar and are distinguished

Table 10
Powder XRD data for high-pressure $Tm_2Si_2O_7$ and $Lu_2Si_2O_7$

h k l	$Tm_2Si_2O_7$				$Lu_2Si_2O_7$			
	Type L[a]		Type B[b]		Type L[a]		Type B[b]	
	d (Å)	I/I_0	*d* (Å)	I/I_0	*d* (Å)	I/I_0	*d* (Å)	I/I_0
0 0 2	8.891	4			8.842	5		
0 1 0	6.547	15	6.56	10	6.515	17	6.478	10
1 0 0	6.544	8			6.516	9		
0 1 1	6.368	13[c]			6.330	13[c]		
1 0 1	6.192	10[c]			6.175	10[c]		
0 −1 1	5.941	6	5.95	3	5.918	6[c]		
			5.80	3				
0 1 2	5.563	3			5.526	3		
1 0 2	5.335	17[c]			5.322	18[c]		
−1 0 2	5.208	2			5.173	2		
0 −1 2	5.022	2			5.003	2		
1 1 0	4.698	3			4.688	2		
0 1 3	4.648	1			4.616	2		
−1 1 0	4.562	2			4.530	3		
−1 1 1	4.480	3			4.444	3		
1 0 3	4.449	28	4.45	15	4.438	30	4.422	10
0 0 4	4.446	3			4.421	4		
1 −1 1	4.360	38	4.35		4.335	40		
−1 0 3	4.339	24		65	4.308	24	4.297	65
1 1 2	4.326	94	4.33		4.318	98		
−1 1 2	4.156	32	4.16	15	4.119	31	4.093	20
−1 0 4	3.635	4			3.609	4		
−1 −1 3	3.523	3			3.509	3		
1 −1 3	3.520	2			3.506	3	3.481	3
1 1 4	3.393	8			3.383	8	3.360	3

[a]Derived from present single-crystal reflection data.
[b]Bocquillon et al. [21].
[c]Reflection diagnostic of type L phase.

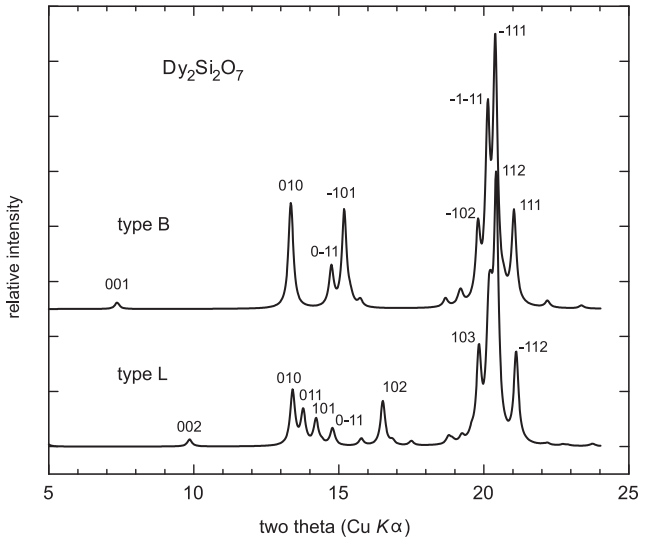

Fig. 6. Calculated partial powder X-ray diffraction patterns of the type B and L polymorphs of $Dy_2Si_2O_7$, identifying weak diagnostic reflections at 13–17° 2θ (Cu$K\alpha$; cf. Table 5): for the type B pattern, the intensity of −1 1 1 is 76 relative to 100 for 0 0 4 and, for type L, the intensity of 1 1 2 is 88 relative to 100 for 0 0 6; powder patterns were calculated using POWDER2 (Penn State University) and crystal-structure data of Fleet and Liu [16,17].

only by rather weak low (2θ) angle reflections (Table 10 and Fig. 6): simulated powder patterns for $Dy_2Si_2O_7$ are used in Fig. 6 because this is the only disilicate with refined structures for both type B and L polymorphs. The geometry of the half-occupied face-shared tetrahedra in the type L structure is consistent with decomposition of a SiO_5 trigonal bipyramid during quenching of the pressure. Therefore, the type L polymorph probably represents a nonquenchable high-pressure phase. Importantly, in this respect, the synthesis conditions for experiments yielding the type L structure lie on the high-pressure side of the stability fields for type B $Tm_2Si_2O_7$ and $Lu_2Si_2O_7$ in Bocquillon et al. [21]. Hence, the phase diagram for $Lu_2Si_2O_7$ (Fig. 5) nicely illustrates the change in structure type from C to D, X, B, and "L" (i.e., C→D→X→B→"L") with progressive increase in pressure, corresponding to progressive decrease in bridging-oxygen bond angle and increase in coordination of Lu^{3+} and, ultimately, in the putative precursor of the type L polymorph (type "L"), to increase in coordination of silicon as well.

Acknowledgments

We thank three reviewers for helpful comments, Michael Jennings for collection of X-ray reflection data, Penny King for use of the piston-cylinder apparatus, R.W. Luth for running the multi-anvil experiments, and the Natural Sciences and Engineering Research Council of Canada for financial support.

References

[1] J. Felsche, J. Less-Common Met. 21 (1970) 1–14.
[2] J. Felsche, Naturwiss 57 (1970) 452.
[3] J. Felsche, Naturwiss 57 (1970) 669–670.
[4] J. Felsche, Z. Kristallogr. 133 (1971) 364–385.
[5] J. Felsche, Naturwiss 59 (1972) 35–36.
[6] Yu.I. Smolin, Yu.F. Shepelev, Acta Crystallogr. B 26 (1970) 484–492.
[7] Y.I. Smolin, Y.F. Shepelev, I.K. Butikova, Sov. Phys. Crystallogr. 15 (1970) 214–219.
[8] O. Greis, H.G. Bossemeyer, P. Greil, B. Breidenstein, A. Haase, Mater. Sci. Forum 79–82 (1991) 803–808.
[9] H.W. Dias, F.P. Glasser, R.P. Gunwardane, R.A. Howie, Z. Kristallogr. 191 (1990) 117–123.
[10] A.N. Christensen, Z. Kristallogr. 209 (1994) 7–13.
[11] A.N. Christensen, R.G. Hazell, Acta Chem. Scand. 48 (1994) 1012–1014.
[12] A.N. Christensen, R.G. Hazell, A.W. Hewat, Acta Chem. Scand. 51 (1997) 37–43.
[13] A.N. Christensen, A.F. Jensen, B.K. Themsen, R.G. Hazell, M. Hanfland, E. Dooryhee, Acta Chem. Scand. 51 (1997) 1178–1185.
[14] M.E. Fleet, X. Liu, Acta Crystallogr. B 56 (2000) 940–946.
[15] M.E. Fleet, X. Liu, J. Solid State Chem. 161 (2001) 166–172.
[16] M.E. Fleet, X. Liu, Z. Kristallogr. 218 (2003) 795–801.
[17] M.E. Fleet, X. Liu, Am. Mineral. 89 (2003) 396–404.
[18] H. Müller-Bunz, T. Schleid, Z. Anorg. Allgem. Chem. 626 (2000) 2549–2556.
[19] H. Müller-Bunz, T. Schleid, Z. Anorg. Allgem. Chem. 628 (2002) 564–569.
[20] I. Hartenbach, F. Lissner, T. Schleid, Z. Naturforsch. 58b (2003) 925–927.
[21] G. Bocquillon, C. Chateau, C. Loriers, J. Loriers, J. Solid State Chem. 20 (1977) 135–141.
[22] Y.I. Smolin, Sov. Phys. Crystallogr. 15 (1970) 36–39.
[23] J. Loriers, G. Bocquillon, C. Chateau, D. Colaïtis, Mater. Res. Bull. 12 (1977) 403–413.
[24] X. Liu, M.E. Fleet, J. Phys.: Condens. Matter 14 (2002) 11223–11226.
[25] J. Ito, Am. Miner. 53 (1968) 890–907.
[26] J. Felsche, J. Solid State Chem. 5 (1972) 266–275.
[27] J.M. Hughes, A.N. Mariano, J.W. Drexler, Neues Jahrb. Mineral. Monatshe. (1992) 311–319.
[28] D.C. Noe, J.M. Hughes, A.N. Mariano, Z. Kristallogr. 206 (1993) 233–246.
[29] M. Takahashi, K. Uematsu, Z.-G. Ye, M. Sato, J. Solid State Chem. 139 (1998) 304–309.
[30] J.E.H. Sansom, D. Richings, P.R. Slater, Solid State Ion. 139 (2001) 205–210.
[31] P. Berastegui, S. Hull, F.J. GarcíaGarcía, J. Grins, J. Solid State Chem. 168 (2002) 294–305.
[32] L. León-Reina, M.C. Martí-Sedeño, E.R. Losilla, A. Cabeza, M. Martíez-Lara, S. Bruque, F.M.B. Marques, D.V. Sheptyakov, M.A.G. Aranda, Chem. Mater. 15 (2003) 2099–2108.
[33] S.R. Bohlen, Neues Jahrb. Mineral. Monatshe. 9 (1984) 404–412.
[34] S.R. Bohlen, A.L. Boettcher, J. Geophys. Res. 87 (1982) 7073–7078.
[35] M.J. Walter, Y. Thibault, K. Wei, R.W. Luth, Canad. J. Phys. 73 (1995) 273–286.
[36] D.A. Sewell, G. Love, V.D. Scott, J. Phys. D 18 (1985) 1233–1243.
[37] Siemens, SHELXTL PC (Version 4.1), Siemens Analytical X-ray Instruments, Inc., Madison, WI, USA, 1993.
[38] J.A. Ibers, W.C. Hamilton (Eds.), International Tables for X-ray Crystallography, vol. IV, Kynoch Press, Birmingham, UK, 1974.
[39] W.H. Zachariasen, Acta Crystallogr. 1 (1948) 263–265.
[40] R.D. Shannon, Acta Crystallogr. A 32 (1976) 751–767.
[41] N.E. Brese, M. O'Keeffe, Acta Crystallogr. B 47 (1991) 192–197.